# Accepted Manuscript


Title: Hardness Prediction in Multi-Pass Direct Diode Laser Heat Treatment by On-Line Surface Temperature Monitoring

Authors: Soundarapandian Santhanakrishnan, Radovan Kovacevic

PII: S0924-0136(12)00181-1
DOI: doi:10.1016/j.jmatprotec.2012.06.002
Reference: PROTEC 13440

To appear in: *Journal of Materials Processing Technology*

Received date: 27-6-2011
Revised date: 30-5-2012
Accepted date: 5-6-2012

Please cite this article as: Santhanakrishnan, S., Kovacevic, R., Hardness Prediction in Multi-Pass Direct Diode Laser Heat Treatment by On-Line Surface Temperature Monitoring, *Journal of Materials Processing Technology* (2010), doi:10.1016/j.jmatprotec.2012.06.002

# Hardness Prediction in Multi-Pass Direct Diode Laser Heat Treatment by On-Line Surface Temperature Monitoring

**Soundarapandian Santhanakrishnan and Radovan Kovacevic***

Research Center for Advanced Manufacturing, Southern Methodist University, Dallas, TX, USA

## Abstract

This study was attempted to develop a process model, using the temperature values measured by the coupled infrared temperature measurement system (pyrometer and camera) correlated with the measured values of case depth hardness of the tool steel AISI S7 (hypo-eutectoid steel) for the specified multi-pass laser heat treatment conditions (1000–2500 J). A number of heat treatment experiments by changing the laser power (1400–1800 W), scanning speed (15–25 mm/s), size of overlap (1–6 mm), and the length of scan (10 – 30 mm) on the tool steel AISI S7 were carried out by using a 2-kW direct diode laser. The results indicated that the loss of case depth hardness uniformity was highly influenced by the tempering temperature and the change of coolling rate. The combination of higher laser power, lower scanning speed, smaller size of overlap, and the longer length of scan were influenced the formation of mixture of phases (martensite, bainite, ferrite, and pearlite) which in turn affected the case depth hardness uniformity. The process model can be used as a handy tool for the process engineers to configure the processing conditions in order to obtain the desired case depth hardness for the hypo-eutectoid steels.

**Keywords**: *high power direct diode laser (HPDDL), laser-based phase transformation hardening (LPTH), multi-pass direct diode laser heat treatment (MPDDLHT), laser-assisted infrared (LAI) pyrometer, infrared camera, process model*

*Corresponding author: Dr. Radovan Kovacevic, Director, Research Center for Advanced Manufacturing and Center for Laser Aided Manufacturing, Southern Methodist University, 3101 Dyer Street, Dallas, TX 75205, USA

E-mail address: kovacevi@lyle.smu.edu, Tel.: +1-214-768-4865; Fax: +1-214-768-0812

## 1. INTRODUCTION

Localized heat treatment (LHT) by a high power direct diode laser (HPDDL) is a relatively new technique. The LHT produces hard and wear-resistant layers only at the selected regions of components, whereas the bulk mass property of the material is retained. Kinkade (2006) briefly reported the advantages of using HPDDL over other high power lasers ($CO_2$, Nd:YAG) for LHT. The HPDDL has a larger focal beam spot (12 mm × 1 mm) with uniform power distribution (top-hat). It operates at a shorter wavelength (808 nm) and provides better beam absorptivity by metals and has higher wall-plug efficiency (~30%). The HPDDL's unit is compact and mobile. In comparison to other lasers processed heat-affected zone (HAZ), its HAZ is minimal.

However, it is challenging to obtain uniform case depth hardness for a larger surface area that is exposed to multiple laser scans. The edges of the previously heat treated area, neighboring the successive laser scan, could undergo different cycles of heating and cooling than the central heat treated region. The non-homogeneity of the heating and cooling cycles and the resultant heat management in the treated material could generate a tempering effect at the edges of the previously hardened zones. The tempering process leads to non-homogeneous phase transformations and non-homogeneity microstructures, resulting in a loss of uniform hardness. Therefore, a process model is necessary to obtain uniform case depth hardness for multi-pass laser heat treatment (MPLHT).

Kasatkin and Vinokur (1984) and Hojerslev (2001) constructed the empirical relationships to calculate the austenization starting ($A_{C1}$) and ending ($A_{C3}$), and the martensite starting ($M_S$) and final ($M_F$) temperatures of steels, respectively. Reti et al. (1987) and Li et al. (1998) presented mathematical models to predict the transformation kinetics such as phase transformations, variation in microstructures, decomposed phases of austenite, and the changes of hardness of the heat-treatable steels for non-isothermal processes. Totten (2006) described the variation in microstructures (carbides, ferrite, cementite, and tempered martensite) of steels with respect to the change of temperatures. Fortunato et al. (2009) and Campana et al. (2009) proposed an optimal multi-pass laser process simulator and statistical method, respectively. The methods were used to determine the hardness uniformity under various laser processing conditions such as the laser power, scanning speed, size of overlap, and the length of scan. Rana et al. (2007) studied the influence of carbon content in steels and laser processing parameters on the variation

in microstructure and hardness, and the results indicated fair hardness uniformity at 30% ratio of overlap.

Smurov et al. (1994), and Smurov and Doubenskaia (2009) have extensively studied the laser-based process monitoring and temperature control via infrared pyrometer. The results were used to determine the rates of heating and cooling for optimizing the physical and metallurgical characteristics of the heat treated materials. Pantsar (2004) used an infrared pyrometer to study the various HPDDL heat treatment conditions. The phase transformations, variations in microstructure, and the changes of hardness were characterized with the aid of differential interference contrast (DIC) images. Xu et al. (2008) used a real-time infrared process monitoring technique and developed a process model. The model has the threshold laser processing values to determine a specified hardness of the heat treated material. Wang et al. (2000) used an infrared camera for surface temperature monitoring for studying the variation in microstructure and phase transformations with respect to the change of processing parameters. Bataille et al. (1990), Derouet et al. (1996), Cook and Haake (2000), and Holmberg and Weiss (2006) reported that the desired case depth hardness with homogeneity microstructure was obtained using a closed-loop process monitoring and control environment.

This study was carried out to develop a case depth hardness prediction model for the AISI S7 tool steel (0.53% C, hypo-eutectoisd steel). The measured surface temperatures by the coupled infrared temperature measurement system for different MPLHT conditions were correlated to the measured values of case depth hardness in order to develop a process model. A set of transformation temperatures such as $A_{C1}$, $A_{C3}$, $M_S$, and $M_F$ were incorporated in this model, that can be used to configure the processing parameters in order to obtain the desired case depth hardness for the hupo-eutectoid steels.

## 2. EXPERIMENTAL SETUP AND PROCEDURES

The study of MPLHT process consisted of three stages: a pre-heat treatment stage, where the coupon was prepared for the study; a heat treatment stage, where the coupon was subjected to the heat treatment; and the third, a post-heat treatment stage, where a metallurgical study and hardness measurements were made.

The tool steel AISI S7 (0.53% C) was used as a candidate material for this study. The chemical composition of the tool steel AISI S7 given by the manufacturer, Bohler-Uddeholm, IL,

USA., is summarized in Table 1. This type of tool steel finds an application in a variety of cutting tools, punches, molds and dies. These tools and dies require only local hardening at the selected regions where they may have to withstand harsh working conditions (involving plastic deformation processes).

Table 1 Chemical compositions of tool steel AISI S7.

| Element | C | Mn | Si | Cr | Mo | V | Cu | P | S |
|---|---|---|---|---|---|---|---|---|---|
| Weight (%) | 0.53 | 0.20-0.80 | 0.20-1.00 | 3.25 | 1.30-1.80 | 0.25 | 0.25 | 0.03 | 0.03 |

An abrasive water jet (AWJ) machine (Flow–IFB 4400) was used to cut the coupons to the size of 50 mm × 35 mm × 10 mm. A surface grinder (Brown & Sharp–Micromaster 618) was used to remove the oxide layer on the top surface of the coupons. Also, the top surfaces of the coupons were sandblasted with aluminum oxide particles in the blasting chamber to increase the laser coupling efficiency. Surface roughness on the top surface of the sandblasted coupons was measured using a roughness measuring instrument (Mitutoyo SJ–201). An average roughness ($R_a$) was recorded as 1.05 μm. To measure the hardness of the top surface, an advanced digital micro-hardness tester (Clark CM–700 AT) was used with a load of 200 gf and dwelling time of 15 s. An average surface hardness value of 210 $HV_{0.2}$ was recorded.

A 2kW HPDDL (Nyvonyx–ISL 2000L) of 808 nm in wavelength, with a rectangular shaped (12 mm × 1 mm) laser spot of an uniformly distributed (top-hat) laser power, was used as a heat source for surface hardening. The beam quality factor value ($M^2$) of 455 and a continuous wave (CW) laser beam mode was used in all the experiments. The laser head was attached to a 6-axis industrial robot (Motoman YR-SK16J00) as shown in Fig. 1a. A water-cooled chiller (Opti Temp) was used to cool the laser head. The Argon shielding gas was used to prevent oxidation at higher temperatures. The power controller of HPDDL was integrated to the robot controller to ensure the control over the laser power, scanning speed, and the time delay between overlapping passes and scanning path. The overall experimental setup is shown in Fig. 1a.

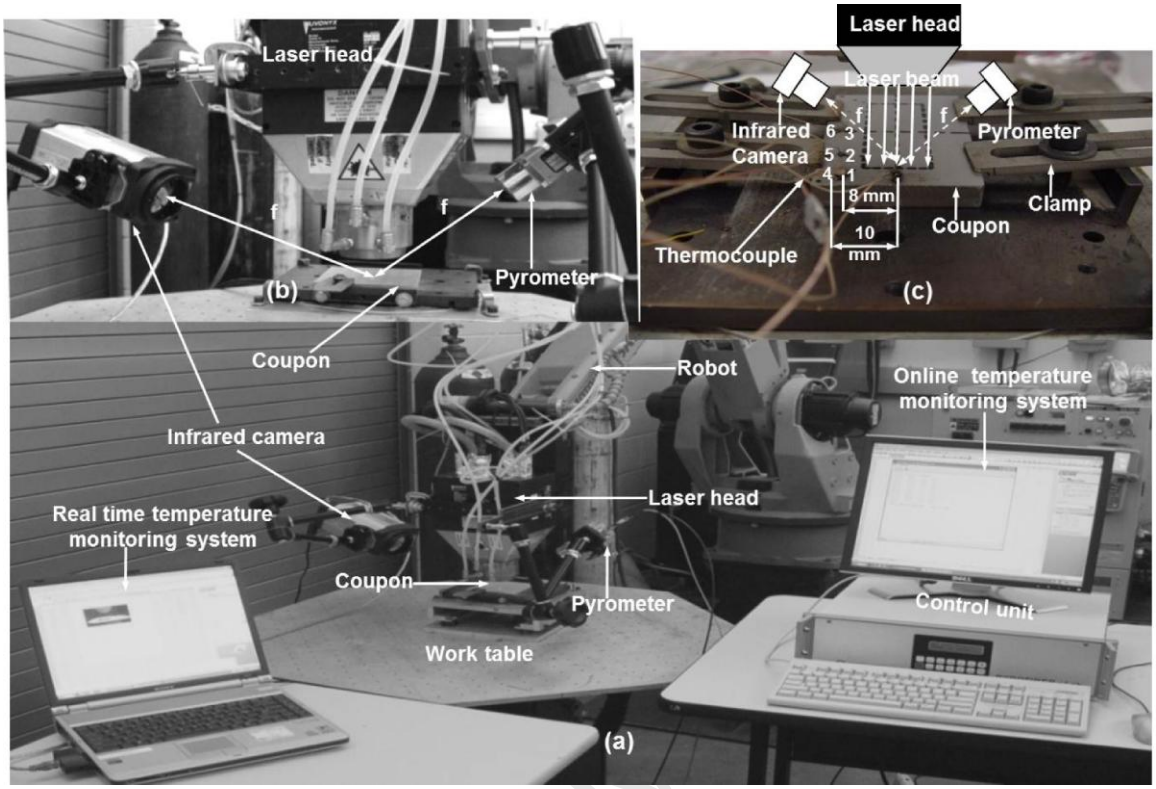


Fig. 1. (a) An overall experimental setup of a real time temperature measurement system, (b) close view of the coupled real time temperature measurement system consists of a laser-assisted infrared pyrometer and infrared camera, and (c) the calibration setup for temperature measurements.

The temperature measurement system coupled with an LAI pyrometer (Pyrofiber®) and infrared camera (FLIR ThermoVision A40) is shown in Fig. 1b. The LAI pyrometer uses a state-of-the-art laser-based technology that in parallel acquires the target surface emissivity and radiance to measure the target temperature more accurately. More technical operating principles of the LAI pyrometer are available in the Pyrometer Instruction Manual (2005). The LAI pyrometer was integrated with the user-friendly software, Pyrofiber®LabVB Remote 2.2, to record the surface emissivity and temperature in real time at a speed of 40 readings/sec. The infrared camera was used to measure the surface temperature up to 2000$^{o}$C at a frame rate of 40 Hz. The infrared camera was integrated with the user-friendly ThermaCAM researcher software (version 2.8 SR3) to obtain the surface temperature in real time. The measured surface emissivity by the LAI pyrometer was used as an emissivity input required for the infrared camera. The emissivity of the surface, distance between the target and the camera, the atmospheric

temperature, and the relative humidity were input in the ThermaCAM researcher software to obtain the surface temperature for various processing conditions.

The temperature measurements by the LAI pyrometer and infrared camera were calibrated with the temperature measurements by the thermocouples. The calibration setup for temperature measurement is shown in Fig. 1 (c). The type-K, NiAl/NiCr thermocouples with a wire diameter of 0.25 mm, shown in Fig. 1 (c), were used to measure the surface temperature. The thermocouples were set at the locations denoted by 1 to 6 shown in Fig. 1 (c). In Fig. 1 (c), the locations denoted by 1 to 3 and 4 to 6 are at the distances of 7 mm and 8 mm from the center of the laser beam, respectively. For the calibration of temperature measurements, the laser power of 1600 W and scanning speed of 20 mm/s were used. The overall mean error was about 3.45%.

The AWJ machine was used for cutting the heat treated coupons to a size of 30 mm × 6 mm × 10 mm. The mounted coupons were polished on the Mark V Lab 3B/4B dual wheel machine by using different GRITs of 120, 240, 400, 600, 800, and 1000 silicon carbide-impeded papers in a plentiful water cleansing environment. Then, the coupons were polished mirror-like on the rotating velvet cloth disc by using alumina powder pastes of 1 µm and 0.05 µm. The coupons were etched with 2% Nital, followed by cleaning the coupons with alcohol.

An ultra high-resolution optical microscope (Keyence VHX–500K) was used to record the cross-sectional micrographs of the etched coupons. The micrographs at the magnification of 200× in a bright field were used to measure the heat treated depth along the tracks ($D_{Tr}$) and overlapped region ($D_{Ov}$). The lineal intercept technique (error could be 3–5%) was used to estimate the $D_{Tr}$ and $D_{Ov}$ in the micrographs. In addition, those micrographs were used to characterize the heat treated zone (HTZ), HAZ, and the base material (BM). A digital micro-hardness tester was used to measure the surface hardness of the heat treated coupons. For all the measurements, a load of 200 gf and dwelling time of 15 s were used to make an indentation on the measuring spot.

## 3. RESULTS AND DISCUSSION

### 3.1 The Effect of Processing Parameters on the Variations of Surface Temperature and Hardness of the Heat Treated Material

The MPLHT is a non-reversible isothermal process, where the phase changes have undergone both the rapid heating and cooling cycles. The physical mechanism of laser-based phase transformation hardening (LPTH) is shown in Fig. 2a. Here, the rapid heating nature of the high power laser beam and the self-quenching effect of the laser exposed regions of the material, producing a hard martensite microstructure that evidently withstands high resistance to heat, wear, and corrosion. The iron-carbon phase and continuous cooling transformation (CCT) diagrams of the tool steel S7 (Bohler-Uddeholm, 2009) are shown in Figs. 2b–c, respectively. In Fig. 2c, due to fast self-quenching, the phase transformations arbitrarily skip the noses of the bainite, ferrite, and pearlite phases to obtain a complete martensite transformation. On the other hand, different phase transformations could be obtained during the continuous laser scanning depending on the variation of cooling rates. The mixture phases will affect the homogeneity of phase transformations, microstructures, and the hardness uniformity.

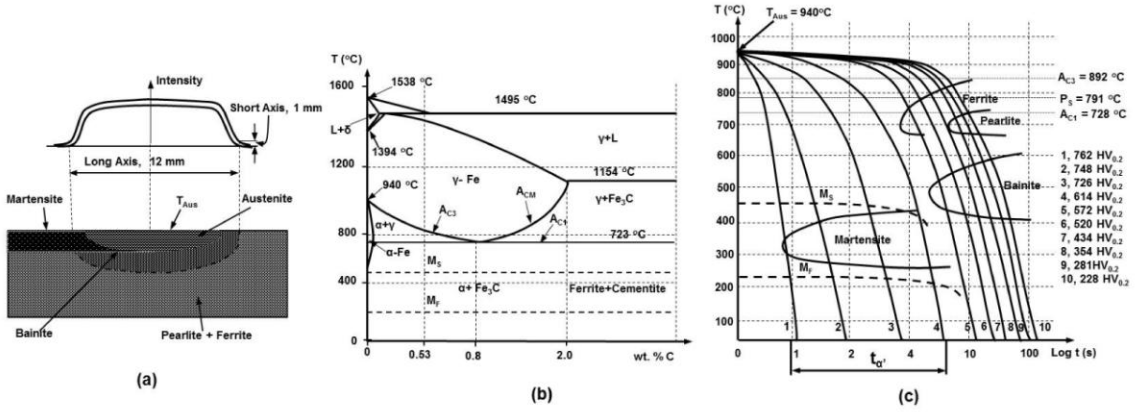


Fig. 2. (a) Physical mechanism of laser-based phase transformation hardening (b) combined with the iron-carbon phase diagram (c) CCT diagram for tool steel AISI S7 (0.53% C).

A simple but a detailed process study was designed to analyze the effect of laser processing parameters on the variation of surface temperature (T, $^{o}$C), tempering temperature ($T_{tmp}$, $^{o}$C), and the hardness of heat treated material ($HV_{0.2}$, kgf/mm$^2$). The tempering temperature is defined as the temperature measured at the overlapped region of the heat treated

surface during the sucessive scans of the laser beam. The scanning path, coupon dimensions, and the size of laser spot are shown in Fig. 3. At the initial stage, the laser power of 1400–1800 W, scanning speed of 15–25 mm/s, size of the overlap of 3 mm, and the length of scan of 25 mm were chosen. Later, the size of overlap of 1 mm to 6 mm, and the length of scan of 10 mm to 30 mm were used for the detailed process study. The infrared temperature measurement system, shown in Fig. 1b, was used to measure the heat treated surface temperature for various MPDDLHT conditions.

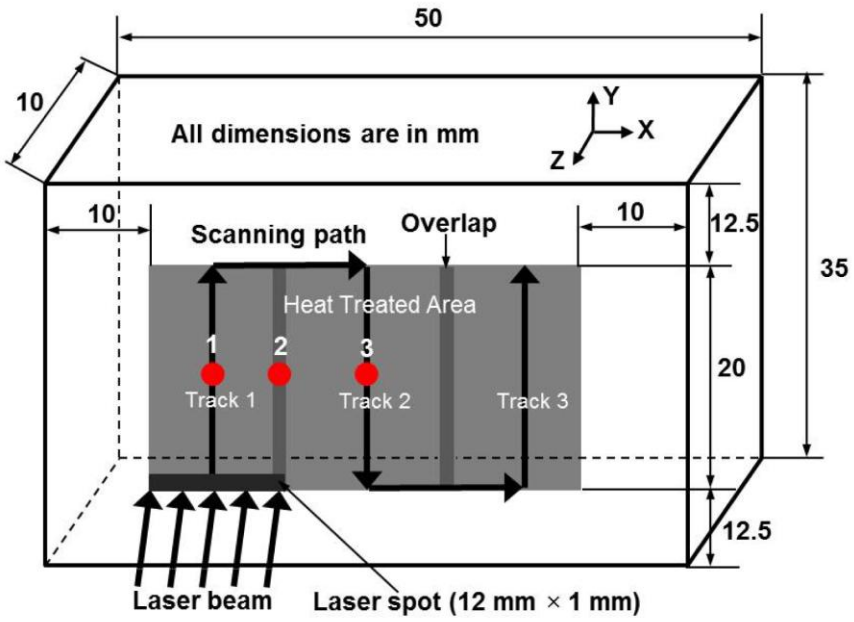


Fig. 3. The schematic presentation of the coupon dimensions and scanning path.

The isotherms (spatial resolution, 200 µm, image frequency, 40 Hz, grid size, 0.25 mm × 0.25 mm, and temperature scale, $^{o}$C) for different MPDDLHT conditions are shown in Figs. 4a–c, respectively. The isotherms were taken during the second scan of the laser beam on the heat treated surface. In Figs. 4a–c, the peak power densities at the center of the laser beam and in the overlapped region shrink while the laser power decreases for the constant scanning speed, size of overlap, and the length of scan. Figs. 4a and 4b clearly show that the average surface temperature at the overlapped region is maintained above the $A_{C1}$ temperature (728$^{o}$C). The higher values of heat input and lower cooling rate could extend the heat accumulation in the overlapped region, resulting in a rising of the surface temperature above the $A_{C1}$ temperature. On the other hand, in

Fig. 4c, the average surface temperature at the overlapped region falls below the $A_{C1}$ temperature due to both the lower heat input and higher cooling rate.

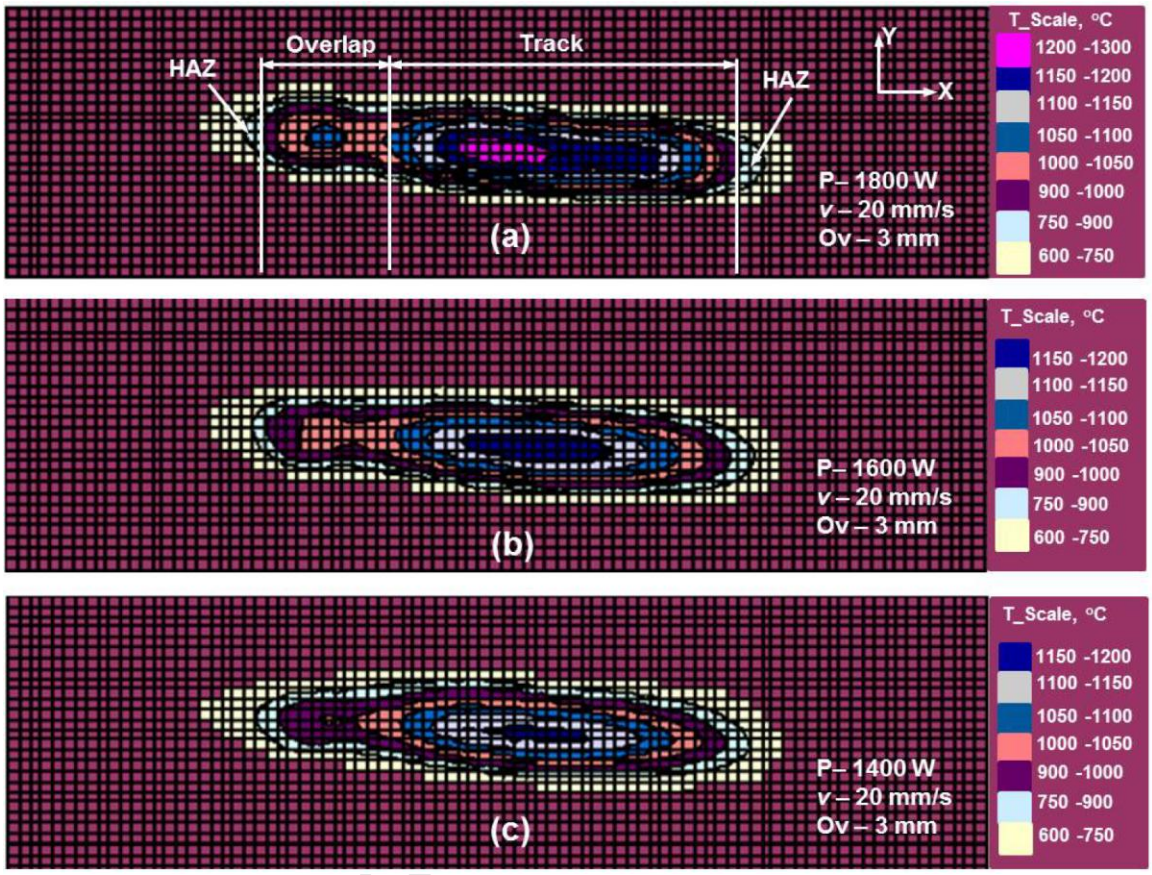


Fig. 4. Real time isotherms of the heat treated coupons for a constant scanning speed (20 mm/s) and size of overlap (3 mm) for various laser powers (a) 1800 W, (b) 1600 W, and (c) 1400 W.

By comparing the isotherms (Figs. 4a–c) with the cross-sectional micrograph (200×) of the heat treated coupon (Fig. 5a), it is easy to distinguish the three regions: HTZ, HAZ, and BM. The scanning electron micrographs (SEM, 2000×) for different locations are shown in Figs. 5b−g. The SEM micrographs were used to distinguish the phase transformations for different MPDDLHT conditions.

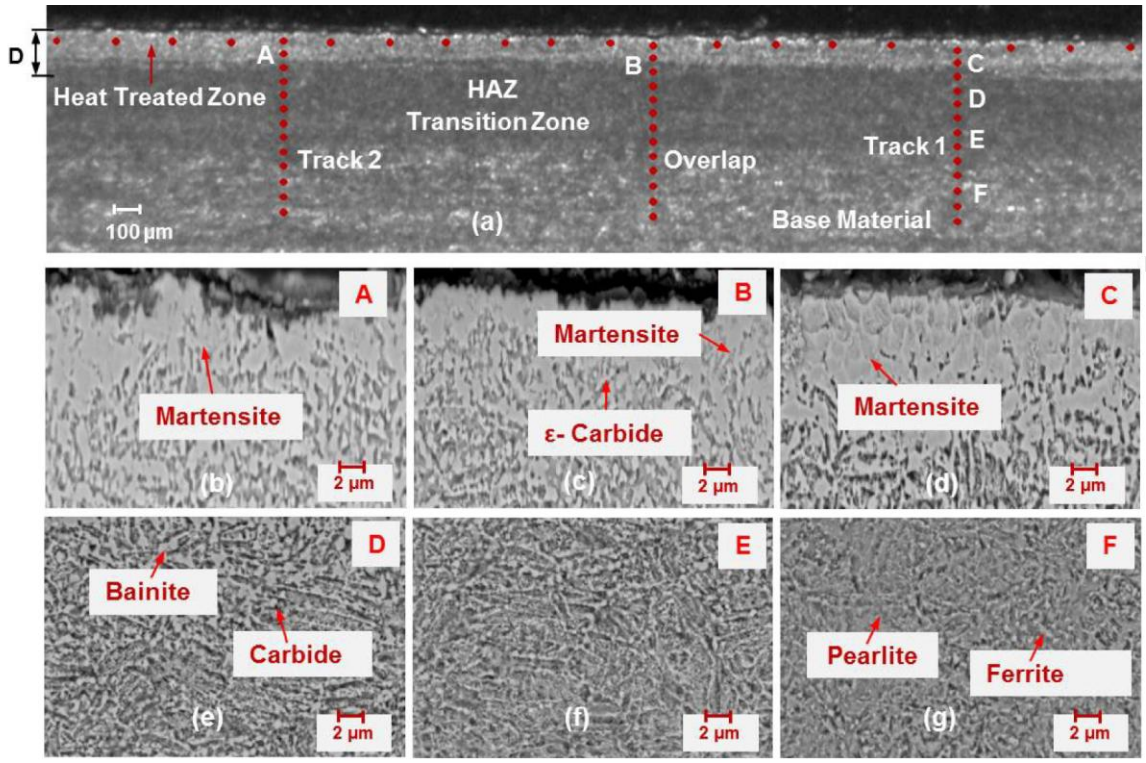


Fig. 5. Micrographs of multi-track laser heat treatment (a) at magnification of 200× (b) – (g) at magnification of 2000×, heat treated zone of (b) first track, (c) overlapped region and (d) second track (e) HAZ (f) transition zone, and (g) base material.

The isothermal grids for different MPDDLHT conditions were used to calculate the surface temperature and tempering temperature. The cross-sectional micrograph (Fig. 5a) was used to measure the heat treated depth along the tracks and overlapped region ($D_{Tr}$, $D_{Ov}$). In Fig. 5a, the spots indicate the positions where the hardness measurements were taken ($HV_{Tr}$, $HV_{Ov}$). The hardness measurement was performed below 25 µm of the top surface of the heat treated coupon. The calculated surface temperatures and tempering temperatures, and the measured heat treated depth and hardness for various MPDDLHT conditions are summarized in Table 2. The recorded values of temperature, heat treated depth, and the hardness at the track are the average values of the first and second tracks (locations 1 and 3 of Fig. 3). Similar average values were recorded for the overlapped regions (location 2 of Fig. 3).

Table 2 The measured values of surface temperature, heat treated depth of material, and the hardness for various laser processing parameters.

| Ex. No | P (W) | *v* (mm/s) | Ov (mm) | Ls (mm) | T (°C) | | | $T_{tmp}$ (°C) | D (μm) | | | $HV_{0.2}$ (kgf/mm²) | | |
|---|---|---|---|---|---|---|---|---|---|---|---|---|---|---|
| | | | | | $T_{Tr}$ | $T_{Ov}$ | ΔT | | $D_{Tr}$ | $D_{Ov}$ | ΔD | $HV_{Tr}$ | $HV_{Ov}$ | ΔH |
| 1 | 1400 | 15 | 3.0 | 25 | 1033 | 982 | 4.93 | 618 | 165 | 150 | 9.09 | 671 | 645 | 3.87 |
| 2 | 1400 | 20 | 3.0 | 25 | 995 | 941 | 5.42 | 571 | 150 | 125 | 16.66 | 652 | 620 | 4.91 |
| 3 | 1400 | 25 | 3.0 | 25 | 956 | 837 | 12.44 | 504 | 140 | 115 | 17.85 | 614 | 542 | 11.72 |
| 4 | 1600 | 15 | 3.0 | 25 | 1148 | 1073 | 6.53 | 795 | 200 | 165 | 17.5 | 776 | 729 | 6.05 |
| 5 | 1600 | 20 | 3.0 | 25 | 1096 | 1057 | 3.55 | 739 | 170 | 160 | 5.88 | 736 | 722 | 1.90 |
| 6 | 1600 | 25 | 3.0 | 25 | 1042 | 945 | 9.30 | 698 | 160 | 135 | 15.62 | 673 | 616 | 8.46 |
| 7 | 1800 | 15 | 3.0 | 25 | 1193 | 1091 | 8.54 | 873 | 200 | 175 | 12.5 | 795 | 740 | 6.91 |
| 8 | 1800 | 20 | 3.0 | 25 | 1145 | 1080 | 5.67 | 812 | 190 | 165 | 13.15 | 763 | 729 | 4.46 |
| 9 | 1800 | 25 | 3.0 | 25 | 1075 | 1029 | 4.27 | 756 | 165 | 150 | 8.82 | 723 | 707 | 2.21 |

P – Laser power, *v* – Scanning speed, Ov – Size of overlap, Ls – Length of scan, T – Surface temperature, $T_{Tr}$ – Average temperature at track, $T_{Ov}$ – Average temperature at overlap, ΔT − Difference of average temperature between the track and overlap, $T_{tmp}$ – Tempering temperature, D – Heat treated depth, $D_{TR}$ – Average heat treated depth at track, $D_{OV}$ – Average heat treated depth at overlap, ΔD − Difference of average heat treated depth between the track and overlap, HV – Hardness, $HV_{TR}$ – Average hardness at track, $HV_{OV}$ – Average hardness at overlap, and ΔHV − Difference of average hardness between the track and overlap.

In Table 2, the experiments 4, 7, and 8 are heat treated at the higher laser power and lower scanning speed. It can be observed that excessive heating and uneven cooling resulted by a higher tempering temperature (above $A_{C1}$) at the overlapped region. In these conditions, an uneven depth of heat treatment and non-uniform hardness distribution between the tracks and overlapped region were achieved. In experiments 2, 3, and 6 (shown in Table 2), the combination of both lower laser power and higher scanning speed was used. A non-homogeneous thermal cycle (lower heating and higher cooling rates) and a relatively lower (below $A_{C1}$) tempering temperature were obtained. These laser processing conditions resulted in larger variations in the case depth hardness. In experiments 1, 5, and 9, both the laser power and scanning speeds generated the balanced heating and cooling cycles. This can be evidently observed by the tempering temperature falling between the $A_{C1}$ and $A_{C3}$ temperatures which in turn achieved a minimum variation in case depth hardness. The more uniform case depth hardness was achieved with the following laser processing parameters: laser power (1400–1600 W) and scanning speed (15–25 mm/s). In the next part, more experimental investigations were carried out for determining the optimal size of overlap and length of scan.

In the MPLHT, the heat management and the resulting tempering process could control the homogeneity of phase transformations, microstructure, and the uniformity of hardness. The heat management is defined by the size of overlap and length of scan. The various size of overlap

and length of scan, and its effect on the surface temperature, tempering temperature, and the hardness are shown in Tables 3 and 4, respectively.

Table 3 The effect of size of overlap on the variation of surface temperature, tempering temperature, and the hardness for a constant laser power of 1600 W and length of scan of 20 mm.

| Ex # | Ov (mm) | T ($^oC$) | | | $HV_{0.2}$ ($kgf/mm^2$) | | |
|---|---|---|---|---|---|---|---|
| | | $T_{Tr}$ | $T_{Ov}$ | $T_{tmp}$ | $HV_{Tr}$ | $HV_{Ov}$ | ΔHV |
| 1 | 1 | 1031.15 | 1009.64 | 617 | 704 | 541 | 163 |
| 2 | 2 | 1028.46 | 1013.25 | 668 | 713 | 601 | 110 |
| 3 | 3 | 1024.82 | 1017.52 | 746 | 725 | 713 | 12 |
| 4 | 4 | 1021.72 | 1034.05 | 811 | 736 | 624 | 112 |
| 5 | 5 | 1026.23 | 1039.42 | 893 | 741 | 572 | 169 |
| 6 | 6 | 1030.61 | 1043.51 | 934 | 749 | 535 | 214 |

Ov – Size of overlap, T – Surface temperature, $T_{Tr}$ – Average temperature at track, $T_{Ov}$ – Average temperature at overlap, $T_{tmp}$ – Tempering temperature, HV – Hardness, $HV_{TR}$ – Average hardness at track, $HV_{OV}$ – Average hardness at overlap, and ΔHV − Difference of average hardness between the track and overlap.

Table 4 The effect of length of scan on the variation of surface temperature, tempering temperature, and the hardness for a constant laser power of 1600 W and size of overlap of 3 mm.

| Ex # | $L_S$ (mm) | T ($^oC$) | | | $HV_{0.2}$ ($kgf/mm^2$) | | |
|---|---|---|---|---|---|---|---|
| | | $T_{Tr}$ | $T_{Ov}$ | $T_{tmp}$ | $HV_{Tr}$ | $HV_{Ov}$ | ΔHV |
| 1 | 10 | 1018.25 | 1038.57 | 893 | 743 | 567 | 176 |
| 2 | 15 | 1014.79 | 1027.36 | 814 | 739 | 625 | 114 |
| 3 | 20 | 1016.16 | 1014.62 | 743 | 726 | 711 | 15 |
| 4 | 25 | 1024.52 | 1007.23 | 659 | 714 | 613 | 101 |
| 5 | 30 | 1019.61 | 1001.15 | 611 | 704 | 539 | 165 |
| 6 | 35 | 1020.85 | 998.35 | 574 | 687 | 476 | 211 |

Ls – Length of scan, T – Surface temperature, $T_{Tr}$ – Average temperature at track, $T_{Ov}$ – Average temperature at overlap, $T_{tmp}$ – Tempering temperature, HV – Hardness, $HV_{TR}$ – Average hardness at track, $HV_{OV}$ – Average hardness at overlap, and ΔHV − Difference of average hardness between the track and overlap.

In Table 3, the temperature at the overlapped region, the tempering temperature, and the hardness at the track increase with the increase in the size of overlap. In contrast, in Table 4, the temperature at the overlapped region, the tempering temperature, and the hardness at the track decrease with the increase in the length of scan. Very interestingly, the hardness at the overlapped region increases up to the size of overlap of 3 mm; above 3 mm, the hardness decreases. A similar trend was observed in the results of the length of scan versus hardness at the overlapped region. Here, the hardness at the overlapped region increases up to the length of 20 mm; above 20 mm of length of scan, the hardness decreases. At a bigger size of overlap (Ov > 3mm) and shorter length of scan ($L_S$ < 20 mm), the heat accumulation at the overlapped region is

high and the resultant cooling rate is low. This result obviously increases the tempering temperature to above the $A_{C1}$ and close to the $A_{C3}$ temperatures.

Referring to the CCT diagram (Fig. 2c), in these cases (Ov > 3mm; $L_S$ < 20 mm), the cooling cycle could skip the nose of the martensite phase transformation, resulting in retaining a portion of austenite. The mixture of retained austenite with the martensite could produce a larger hardness variation between the track and overlapped region. For a smaller size of overlap (Ov < 3mm) and longer length of scan ($L_S$ > 20 mm), the tempering temperature falls below the $A_{C1}$ temperature. The reason could be a lesser amount of heat accumulation and higher rate of cooling, resulting in a partial austenization that consists of a mixture of phases of bainite, ferrite, and pearlite. This causes a larger hardness variation between the track and overlapped region. A balanced thermal cycle, full martensite transformation, and more uniform hardness were achieved at a size of overlap of 3 mm and length of scan of 20 mm. A minimum variation of surface temperature and the case depth hardness between the track and overlapped region were obtained under the following processing window: the laser power (1400–1800 W), scanning speeds (15–25 mm/s), size of overlap of 3 mm, and the length of scan of 20 mm.

It can be concluded that in the MPDDLHT, the hardness uniformity is a function $[f\ (HV) = f\ (T_{tmp})]$ of the tempering temperature. The tempering temperature is a function $[f\ (T_{tmp}) = f\ (Ov, Ls)]$ of the size of overlap and length of scan. Therefore, the hardness uniformity is a function $[f\ (HV_{Uniformity}) = f\ (Ov, Ls, P, v)]$ of the size of overlap, length of scan, laser power, and the scanning speed.

Referring to Figs. 2, 4, and 5, three different surface conditions were observed:

*Case 1*: ($T_{tmp}$ > $A_{C1}$). For a bigger size of overlap (Ov > ¼ of $L_{HPDDL}$; here $L_{HPDDL}$ is 12 mm) and shorter length of scan ($L_S$ < 2 times of $L_{HPDDL}$), the tempering temperature is above the $A_{C1}$ temperature. A higher heating and reaustenization have occured. A portion of austenite and martensite mixture has been obtained.

*Case 2*: ($A_{C1}$ < $T_{tmp}$ < $A_{C3}$). For a medium size of overlap (Ov = ¼ of $L_{HPDDL}$) and length of scan ($L_S$ ≈ 2 times of $L_{HPDDL}$), tempering temperature falls between the $A_{C1}$ and $A_{C3}$ temperatures. A full austenization occurs in the heat treated material; then by rapid cooling, a complete martensite transformation was achieved.

*Case 3*: ($T_{tmp}$ < $A_{C1}$). For a smaller size of overlap (Ov < ¼ of $L_{HPDDL}$) and longer length of scan ($L_S$ > 2 times of $L_{HPDDL}$), tempering temperature falls below the $A_{C1}$ temperature. A partial

austenization occurs; then by controlling the cooling cycle, a mixture of phases (bainite, ferrite, and pearlite) was obtained.

### 3.2 Discussion on the Effect of Processing Parameters on the Variation of Temperature, Phase Transformations, and Change of Hardness

In the MPDDLHT, the heat treated surface temperature is dependent on the given laser processing parameters. The final hardness of the heat treated material is dependent on the phase changes caused by the level of carbon solubility during the heating and cooling cycles. Therefore, a detailed experimental investigation was carried out to quantify the effect of laser heat treatment processing parameters on the variation of thermal cycles, phase transformations, and the hardness.

The references Kasatkin and Vinokur (1984), Hojerslev (2001), and Li et al. (1998) were used to calculate the transformation temperatures ($A_{C1}$, $A_{C3}$, $B_S$, $P_S$, $M_S$ and $M_F$) of tool steel AISI S7. The laser powers of 1400 W, 1600 W, and 1800 W for a constant scanning speed of 20 mm/s, size of overlap of 3 mm, and the length of scan of 20 mm were used for the experimental investigations. The recorded thermal cycles, micrographs (200×), tempering cycles, and the hardness at tracks and overlapped region for various MPDDLHT conditions are shown in Figs. 6–8.

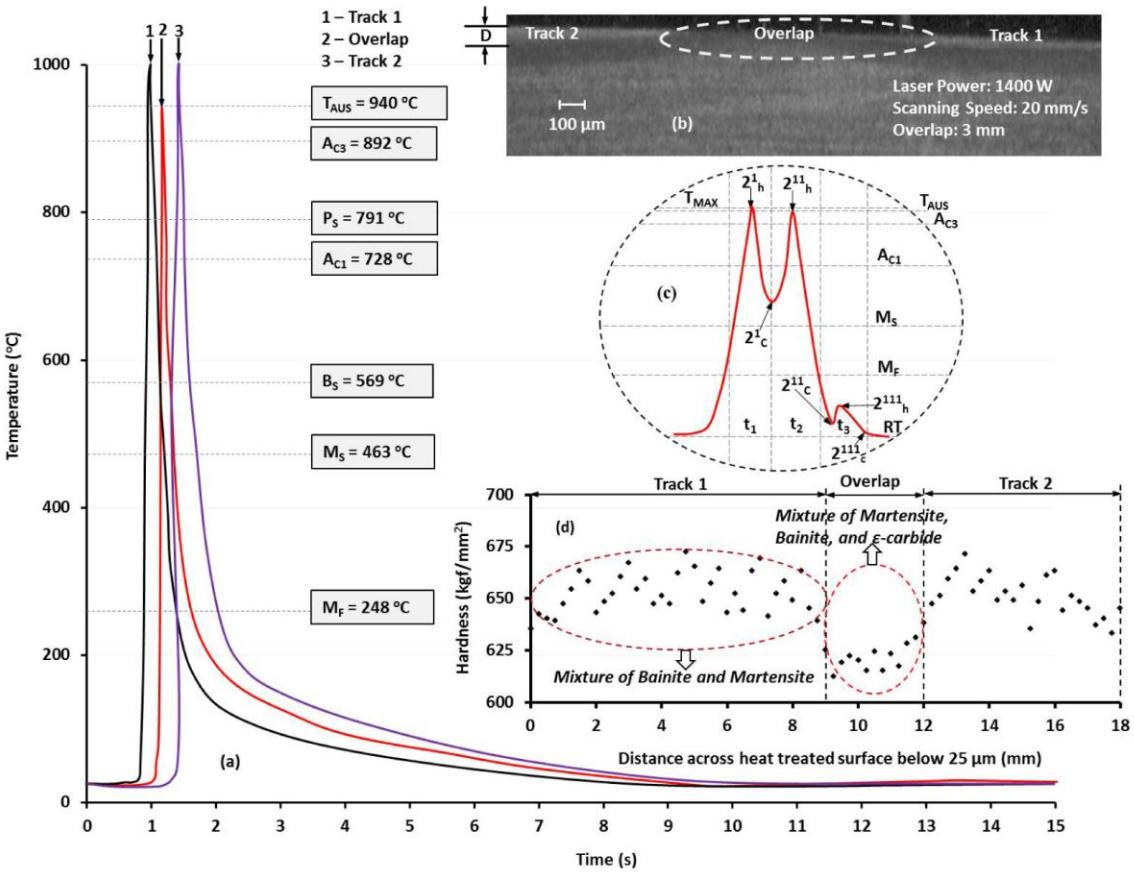


Fig. 6. (a) Temperature history of the heat treated coupon at the laser power of 1400 W, scanning speed of 20 mm/s, and the size of overlap of 3 mm, (b) micrograph (200×), (c) temperature history at the overlapped region, (d) surface hardness distribution.

In Fig. 6a, at a lower laser power, a minimum heat generation, and a higher cooling rate, a larger peak surface temperature variation between the tracks and overlapped region is observed. Upon a closer look, the overlapped region's thermal cycle reaches below the $A_{C1}$ temperature. Again the thermal cycle is led by successive laser scanning that could accumulate minimum heat in that region. But a contrasting higher cooling rate results in a non-uniform peak surface temperature variation between the tracks and overlapped region. In Fig. 7a, at higher laser power, a larger variation of peak surface temperature among the locations 1 to 3 is observed. This larger variation could be the result of the extension of the overlapped region's heat accumulation to the neighboring successive laser scanning track. However, in Fig. 8a, a minimum variation of peak surface temperature is observed due to the balanced heating and cooling cycles. In this case, the overlapped region's tempering temperature is maintained above the $A_{C1}$ temperature.

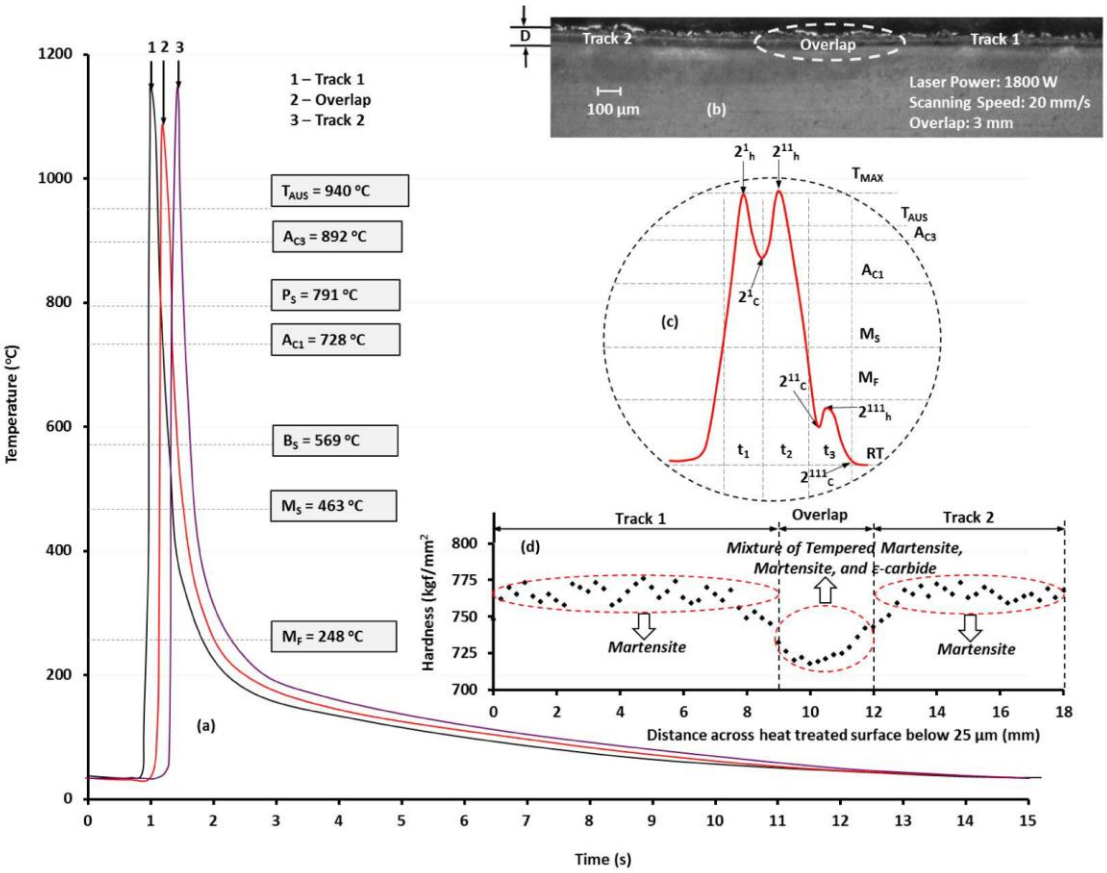


Fig. 7. (a) Temperature history of the heat treated coupon at the laser power of 1800 W, scanning speed of 20 mm/s, and the size of overlap of 3 mm, (b) micrograph (200×), (c) temperature history at the overlapped region, (d) surface hardness distribution.

The temperature history at the overlapped region was plotted to quantify the effect of the processing parameters on the variation of the surface temperature and the corresponding tempering effect. The overlapped region's thermal cycles for different MPDDLHT contions are shown in Figs. (6–8)c. In Figs. (6–8)c, $2_h^1$, and $2_c^1$ are the peak temperatures of the heating and cooling cycles during the first scan of the laser beam. Similarly, $2_h^{11}$, $2_c^{11}$, $2_h^{111}$, and $2_c^{111}$ are the peak temperatures of the heating and cooling cycles during the second and third scans of the laser beam, respectively. The $t_1$, $t_2$, and $t_3$ are the times taken for the heat treatment cycles during the first, second, and the third scans of the laser beam, respectively.

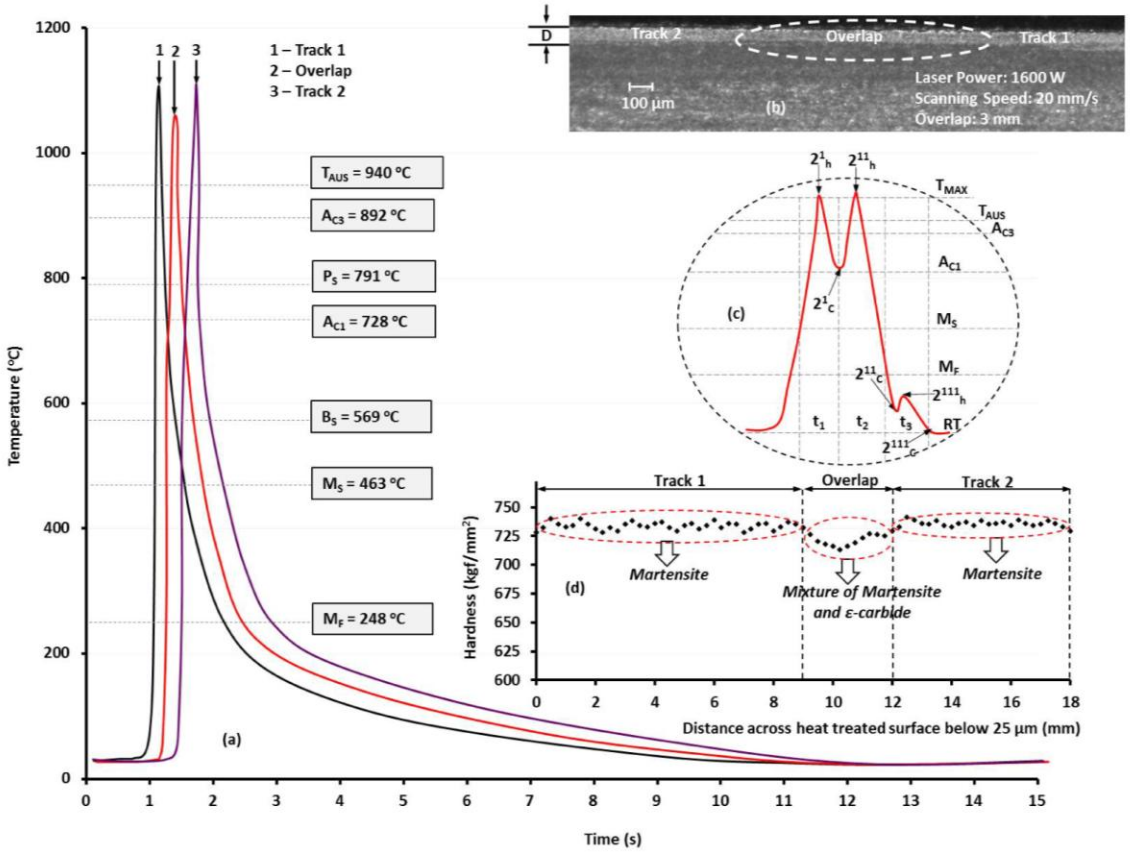


Fig. 8. (a) Temperature history of the heat treated coupon at the laser power of 1600 W, scanning speed of 20 mm/s, and the size of overlap of 3 mm, (b) micrograph (200×), (c) temperature history at the overlapped region, (d) surface hardness distribution.

In Fig. 6c, the peak temperatures at the locations of $2_h^1$, $2_h^{11}$, and $2_h^{111}$ are 995°C, 941°C, and 110°C, respectively. The peak temperatures at the locations of $2_c^1$, $2_c^{11}$, and $2_c^{111}$ are 571°C, 50°C, and 25°C, respectively. The overlapped region's heating ($2_h^{1-111}$) and cooling ($2_c^{1-111}$) thermal cycles were referred to in Figs. 2(b–c) and 5 to determine the phase transformations, microstructures, and the hardness. Here, the tempering temperature is below the $A_{C1}$ temperature, and the time ($t > t_{\alpha^1}$) allowed for diffusion of carbon in the austenite passes through the noses of bainite, ferrite and pearlite. At the end of the cooling cycle ($2_c^{111}$), the metastable martensite already formed in the overlapped region will decompose into the phases of bainite and ε-carbide as the product of solid phase transformation. Thus, the mixture of martensite, bainite, and ε-carbide phases were achieved.

In Fig. 7c, the peak temperatures at the locations of $2_h^1$, $2_c^1$, $2_h^{11}$, $2_c^{11}$, $2_h^{111}$, and $2_c^{111}$ are 1145°C, 812°C, 1080°C, 140°C, 215°C, 25°C, respectively. In this case, a higher heating (see Fig.

8b) and a larger variation of tempering temperatures were obtained. The tempering temperature during the second scan of the laser beam is above the $A_{C1}$ temperature but near the $A_{C3}$ temperature. In this higher tempering temperature ($T_{tmp} > A_{C1}$), the time ($t < t_{\alpha^1}$) taken for diffusion of carbon in the austenite was not enough. Therefore, a portion of retained austenite was mixed with the martensite. On the other hand, at the end of the cooling cycle ($2_c^{111}$), the tempering temperature falls to 140°C. Therefore, a mixture of phases of a portion of retained austenite, martensite, and ε-carbide was achieved.

In Fig. 8c, the peak temperatures at the locations of $2_h^1$, $2_c^1$, $2_h^{11}$, $2_c^{11}$, $2_h^{111}$, and $2_c^{111}$ are 1096°C, 739°C, 1057°C, 90°C, 160°C, 25°C, respectively. In this case, during the second scan of the laser beam, the tempering temperature (739°C) is above the $A_{C1}$ temperature, and the balanced heating and cooling cycles ($t \approx t_{\alpha^1}$) were also obtained . While in the third scan of the laser beam, the temperature drastically falls to 90°C. Referring to Figs. 2(b–c) and 5c, for these tempering temperatures and the cooling cycle time, in addition to martensite, a small portion of martensite was decomposed into the phase of ε-carbide. Therefore, at the end of the cooling cycle ($2_c^{111}$), a mixture of the phases of martensite and ε-carbide was achieved.

The cross-sectional micrographs of the heat treated coupons are presented in Figs. (6–8)b. In Fig. 6b, a larger variation of heat treated depth of material is noticed. In Fig. 7b, a higher heating and uneven heat treated depth of material is presented. On the other hand, a minimum variation of heat treated depth of material was obtained at the laser power of 1600 W, scanning speed of 20 mm/s, size of overlap of 3 mm, and the length of scan of 20 mm, as shown in Fig. 8b.

The measured surface hardness for various MPDDLT conditions are presented in Figs. (6–8)d. In all cases, a similar trend of decrease in hardness was observed in the overlapped region compared to the track. This could be the variation of transformation temperatures ($A_{C1} \rightarrow A_{C3}$) and the subsequent tempering process. In Figs. (6, 7)d, the drastic variation of surface hardness is due to a larger variation in tempering temperatures (see Figs. (6, 7)c). In Fig. 6d, the tempering process ($T_{tmp} < A_{C1}$) could generate a mixture of bainite and ε-carbide that results in a significant hardness reduction in the overlapped region. In Fig. 7d, the tempering temperature is near the $A_{C3}$ temperature, resulting in a portion of retained austenite mixed with the hardened martensite. The mixture phases have generated a hardness decrease in the overlapped region.

In Fig. 8d, a fairly uniform hardness is observed. In this case, the accumulated heat in the overlapped region (see Fig. 8c) contributes to a minimum variation in surface. The thermal cycle (temperature, 90$^{o}$C, and time for cooling, 1.5 s) observed in the overlapped region (see Fig. 8c) could generate a mixture of martensite and ε-carbide. The mixture of martensite and ε-carbide could show a fairly uniform hardness.

### 3.3 Process Model for Predicting Hardness in Heat Treated Material

In Fig. 9a, the effect of the processing parameters such as laser power and scanning speed for a fixed size of overlap and length of scan on the variation of surface temperature is presented. The surface temperature increases with the increase in laser power while it decreases with the increase in the scanning speed. In order to simplify the analysis, a single term heat input (HI) was used. Eq. 3 was used to calculate the values of heat input.

$$HI = P \times \frac{L_S}{v} \tag{3}$$

where HI is the heat input (J), P is the laser power (W), $L_S$ is the length of scan (mm), and $v$ is the scanning speed (mm/s).

Fig. 9b shows the variation of surface temperature versus change of heat input. The surface temperature increases with the increase in the values of heat input. The variation of transformation temperatures ($A_{C1}$, $A_{C3}$, and $T_{AUS}$) and the micrographs, shown in Figs. (6–8)b, were used to plot the different heat treatment regions, shown in Fig. 9a. The austenization above the $A_{C3}$ and $T_{AUS}$ temperatures is shown with shading in Fig 9a. An excessive heating occurs far above the $T_{AUS}$ temperature. Below the $A_{C1}$ temperature, there is no austenization.

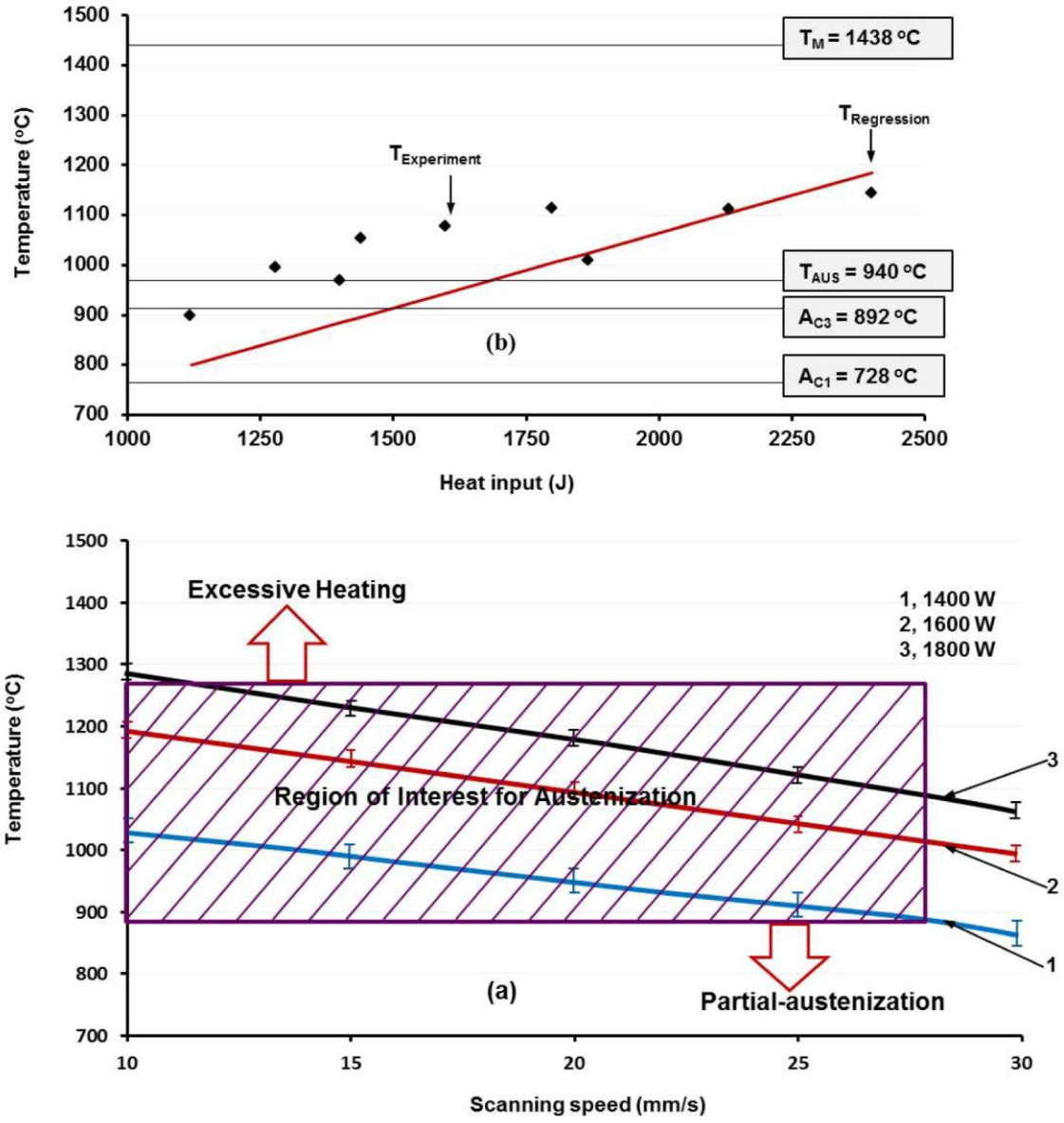


Fig. 9. (a) The effect of processing parameters on the variation of surface temperature, (b) heat input vs. surface temperature.

A process diagram (Fig. 10) was drawn by using the surface temperatures and the measured values of case depth hardness for different MPDDLHT conditions. The two sets of experimental data (temperature versus heat treated depth and temperature versus hardness) were correlated using a polynomial curve fitting method to obtain the emprical relationships. The emprical coefficients in the relationships were further converted into the values which represent the difference ($A_{C3}-A_{C1}$; $M_S-M_F$) and the product [$(A_{C3}-A_{C1})\times(M_S-M_F)$] of transformation

temperatures. Then, the emprical equations (Eqs. 4−6) based on transformation temperatures were designed to calculate the temperature, heat treated depth, and the hardness for the specified laser heat treatment conditions (1000−2500 J).

$$T = \frac{A_{C3} - A_{C1}}{C_1} \times HI + M_S \quad (4)$$

$$D = \frac{1}{C_2}(A_{C3} - A_{C1}) \times HI \times (M_S - M_F) \quad (5)$$

$$HV = \frac{1}{C_3}(A_{C3} - A_{C1}) \times HI \times (M_S - M_F) + HV_{BM} \quad (6)$$

where T is the surface temperature ($^oC$), $A_{C3}$ is the upper critical temperature, D is the heat treated depth of material (μm), $M_S$ and $M_F$ are the martensite starting and final temperatures ($^oC$), respectively, HV is the surface hardness (kgf/mm$^2$), $HV_{BM}$ is the base material hardness (kgf/mm$^2$), and $C_1$ (545, J), $C_2$ (645, J$^o$C/μm) and $C_3$ (380 J $^o$C kgf/mm$^2$) are empirical constants.

The heat treated depth of material and hardness increase with the increase in temperature (Fig. 10). The phase transitions were superimposed with the aid of SEM micrographs (Figs. 5b–g) on the process diagram to determine different regions of heat treatment. Furthermore, the heat treatment regions were distinguished by the variation of transformation temperatures ($A_{C1}$, $A_{C3}$, $M_S$, and $M_F$). No austenization occurs below the $A_{C1}$ temperature. A partial austenization was observed between the $A_{C1}$ and $A_{C3}$ temperatures. A complete austenization was observed above the $A_{C3}$ and $T_{AUS}$ temperatures. This process model can be served as a cost-effective tool for the process engineers to configure the MPDDLHT conditions in order to obtain the desired case depth hardness.

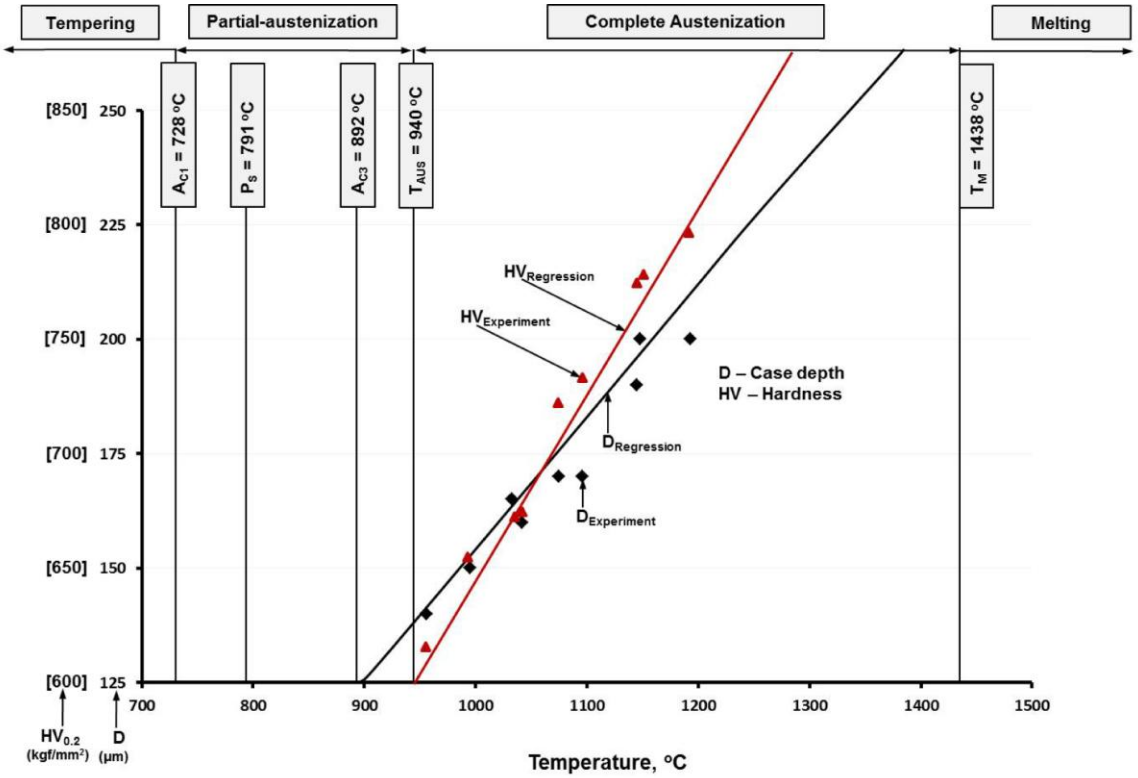


Fig. 10. The effect of surface temperature on the variation of heat treated depth of material and hardness.

## 4. CONCLUSIONS

The MPDDLHT results showed the case depth hardness uniformity was highly influenced by the tempering temperature and the change of cooling rate. The tempering temperature was dependent on the heat management defined by the size of overlap and length of scan. A bigger size of overlap (> ¼ of $L_{HPDDL}$) and shorter length of scan (< 2 × $L_{HPDDL}$) resulted in excessive heating and reaustenization (mixture of a portion of austenite and martensite). The excessive heating and reaustenization caused a non-uniform case depth hardness. The smaller size of overlap (< ¼ of $L_{HPDDL}$) and longer length of scan (> 2 × $L_{HPDDL}$) generated the tempering and mixture phases of bainite, ferrite, and pearlite. The mixture phases could resulted in a loss in the uniformity of case depth hardness. When the size of overlap was equal to ¼ of $L_{HPDDL}$ (12 mm), and the length of scan was equal to 2 × $L_{HPDDL}$, a full austenization and martenisite transformation and more uniform case depth hardness were achieved. The uniformity in case depth hardness was achieved by the following processing parameters window: the laser power

(1400–1800 W), scanning speed (15–25 mm/s), size of overlap of 3 mm, and the length of scan of 20 mm. The measured temperatures readings by the infrared pyrometer and camera were calibrated with the data obtained by the thermocouples. The results indicated a close agreement (error, 3.45 percent). The surface temperatures recorded by the infrared temperature measurement system for different MPDDLHT were correlated with the measured values of heat treated depth and hardness to develop the process model. The process model can be used as a handy tool for the process engineers to configure the MPDDLHT parameters in order to obtain the desired case depth hardness of the hypo-eutectoid steels for the specific processing conditions (1000 −2500 J).

**Glossary of Terms**

HPDDL – High power direct diode laser
$CO_2$ – Carbon di-oxide laser
Nd:YAG – Neodymium-doped yttrium aluminum garnet laser
LPTH – Laser-based phase transformation hardening
MPLHT – Multi-pass laser heat treatment
MPDDLHT – Multi-pass direct diode laser heat treatment
cw – Continuous wave
HTZ – Heat-treated zone
HAZ – Heat-affected zone
BM – Base material
DIC – Differential interference contrast image
LAI – Laser-assisted infra-red pyrometer
NiAl/NiCr - Nickel-aluminum/nickel-chromium
PVC – Polyvinyl chloride
Ra – Average roughness (μm)
t – Time (s)
HI – Heat input (J)
Q – Activation energy (KJ/mol)
R – Gas constant (8.314472 J/$^oC$)
A – Material constant
m – Material constant
P – Laser power (W)
*v* – Scanning speed (mm/s)
$L_S$ – Length of scan (mm)
Ov – Size of overlap (mm)
T – Surface temperature ($^oC$)
$T_{tmp}$ – Tempering temperature ($^oC$)
$T_{Tr}$ – Surface temperature at track ($^oC$)
$T_{Ov}$ – Surface temperature at track ($^oC$)
$\Delta T$ – Difference of temperature between track and overlap ($^oC$)

$A_{C1}$ – Austenization starting temperature ($^oC$)
$A_{C3}$ – Austenization finish temperature ($^oC$)
$P_S$ – Pearlite starting temperature ($^oC$)
$B_S$ – Bainite starting temperature ($^oC$)
$M_S$ – Martensite starting temperature ($^oC$)
$M_F$ – Martensite finish temperature ($^oC$)
$T_{AUS}$ – Austenization temperature ($^oC$)
$T_M$ – Temperature at melting ($^oC$)
D – Heat-treated depth of material (µm)
$D_{Tr}$ – Heat-treated depth of material at track (µm)
$D_{Ov}$ – Heat-treated depth of material at overlap (µm)
ΔD – Difference of heat treated depth between the track and overlap (µm)
HV – Surface hardness ($kgf/mm^2$)
$HV_{Tr}$ – Surface hardness at track ($kgf/mm^2$)
$HV_{Ov}$ – Surface hardness at overlap ($kgf/mm^2$)
ΔHV – Difference of hardness between the track and overlap ($kgf/mm^2$)
$HV_I$ – Initial surface hardness ($kgf/mm^2$)
$HV_F$ – Final surface hardness ($kgf/mm^2$)
$HV_{BM}$ – Base material hardness ($kgf/mm^2$)
$C_1$ – Constant (545 J)
$C_2$ – Constant (645 $J^oC/µm$)
$C_3$ – Constant (380 $J^oC\ kgf/mm^2$)

## ACKNOWLEDGEMENTS

This work was partially funded by NSF Grant # IIP-1034652. The authors greatly acknowledge the help of Andrew Socha, Research Engineer of SMU's Research Center for Advanced Manufacturing (RCAM) for the experimental setup, Dr. Fanrong Kong, Research Engineer of SMU's RCAM and Dr. Shiva Gadag, former Ph. D student of SMU's RCAM, for their valuable comments on this work, and Prof. John Wheeler, Director of ESL, SMU for proof reading the manuscript.

## References

Bataille, F., Kechemair, D., Pawlovski, C., Houdjal, R., 1990. Thermal regulation applied to $CO_2$ laser self quenching of complex geometry workpieces. SPIE Eight Internatinal Symposium on Gas Flow and Chemical Lasers 1397, 839–842.

Bohler Uddeholm United States., 2009. Uddholm Ramax, LH, Stainless Mold Base Steel, www.bucorp.com, Accessed November 2009.

Campana, G., Ascari, A., Tani, G., 2009. A method for laser heat treatment efficiency evaluation in multi-track surface hardening. ASME International Manufacturing Science and Engineering Conference (MSEC 2009) - Symposium of High Power Density Surface Treatments MSEC2009-84095, 1–7.

Cook, C. M., Haake, J.M., 2000. Monitoring and controlling the temperature in a high power direct diode laser surface hardening application. 20th ASM Heat Treating Society Conference Proceedings, 183–191.

FLIR ThermoVision A40 Manual, 2004.

Fortunato, A., Orazi, L., Tani, G., 2009. A new computationally efficient model for tempering in multi-tracks laser hardening. ASME International Manufacturing Science and Engineering Conference (MSEC 2009) - Symposium of High Power Density Surface Treatments MSEC2009-84093, 1–9.

Hojerslev, C., 2001. Tool steels. Riso National Laboratory, Roskilde.

Homberg, D., Weiss, W., 2006. PID control of laser surface hardening of steel. IEEE Transactions on Control Systems Technology 14 (5), 896–904.

Kasatkin, O.G., Vinokur, B.B., 1984. Calculation models for determining the critical points of steel. Metal Science and Heat Treatment 26 (1–2), 27–31.

Kinkade, K., 2006. Diode lasers test their mettle in surface treatment. Laser Focus World, 95–97.

Li, M.V., Niebuir, D.V., Meekiho, L.L., Atteridge, D.G., 1998. A computational model for the prediction of steel hardenability. Metallurgical and Materials Transactions B 29B, 661–672.

Pantsar, H., 2004. Use of DIC in examining phase transformations in diode laser surface hardening. Proceedings of the 23rd International Congress on Applications of Lasers and Electro-Optics (ICALEO 2004), 1–8.

Pyrofiber®., Pyrometer Instruction Manual, 2005.

Rana, J., Goswami, G.L., Jha, S.K., Mishra, P.K., Prasad, B.V.S.S.S., 2007. Experimental studies on the microstructure and hardness of laser-treated steel specimens. Optics & Laser Technology 39, 385–393.

Reti, T., Gergely, M., Tardy, P., 1987. Mathematical treatment of non-isothermal transformations. Materials Science and Technology 3 (5), 365–371.

Totten, G. E., 2006. Steel heat treatment handbook: Metallurgy and technologies. CRC Taylor & Francis, Oregon, USA.

Smurov, I., Doubenskaia, M., 2009. Optical sensing in laser machinig. Proceedings of SPIE:Optical Sensor 7356, 73560T-1–12.

Smurov, I., Martino, V., Ignatiev, M., Flamant, G., 1994. On-line thermocycles measurements in laser applications. Journal DE PHYSIQUE IV 4, C4-147–150.

Wang, X., Takacs, J., Krallics, G., Szilagyi, A., Markovits, T., 2000. Experiemntal research on laser-material interaction. Periodica Polytechnica Ser. Transp. Eng 28 (1-2), 143–152.

Xu, Z., Leong, K. H., Reed, C. B., 2008. Nondestructive evaluation and real-time monitoring of laser surface hardening. Journal of Materials Processing Technology 206, 120–125.